

## Atmospheric Circulation and Its Effect on Arctic Sea Ice in CCSM3 Simulations at Medium and High Resolution\*

ERIC DEWEAVER AND CECILIA M. BITZ

*Department of Atmospheric and Oceanic Sciences, University of Wisconsin—Madison, Madison, Wisconsin*

(Manuscript received 24 January 2005, in final form 30 August 2005)

### ABSTRACT

The simulation of Arctic sea ice and surface winds changes significantly when Community Climate System Model version 3 (CCSM3) resolution is increased from T42 ( $\sim 2.8^\circ$ ) to T85 ( $\sim 1.4^\circ$ ). At T42 resolution, Arctic sea ice is too thick off the Siberian coast and too thin along the Canadian coast. Both of these biases are reduced at T85 resolution. The most prominent surface wind difference is the erroneous North Polar summer anticyclone, present at T42 but absent at T85.

An offline sea ice model is used to study the effect of the surface winds on sea ice thickness. In this model, the surface wind stress is prescribed alternately from reanalysis and the T42 and T85 simulations. In the offline model, CCSM3 surface wind biases have a dramatic effect on sea ice distribution: with reanalysis surface winds annual-mean ice thickness is greatest along the Canadian coast, but with CCSM3 winds thickness is greater on the Siberian side. A significant difference between the two CCSM3-forced offline simulations is the thickness of the ice along the Canadian archipelago, where the T85 winds produce thicker ice than their T42 counterparts. Seasonal forcing experiments, with CCSM3 winds during spring and summer and reanalysis winds in fall and winter, relate the Canadian thickness difference to spring and summer surface wind differences. These experiments also show that the ice buildup on the Siberian coast at both resolutions is related to the fall and winter surface winds.

The Arctic atmospheric circulation is examined further through comparisons of the winter sea level pressure (SLP) and eddy geopotential height. At both resolutions the simulated Beaufort high is quite weak, weaker at higher resolution. Eddy heights show that the wintertime Beaufort high in reanalysis has a barotropic vertical structure. In contrast, high CCSM3 SLP in Arctic winter is found in association with cold lower-tropospheric temperatures and a baroclinic vertical structure.

In reanalysis, the summertime Arctic surface circulation is dominated by a polar cyclone, which is accompanied by surface inflow and a deep Ferrel cell north of the traditional polar cell. The Arctic Ferrel cell is accompanied by a northward flux of zonal momentum and a polar lobe of the zonal-mean jet. These features do not appear in the CCSM3 simulations at either resolution.

### 1. Introduction

With its triple role as shortwave optical reflector, air–sea flux barrier, and freshwater transporter, Arctic sea ice plays a key role in simulations of anthropogenic climate change. As a recent example, Holland and Bitz (2003) found that climate models with relatively thin sea ice showed more Northern Hemisphere polar am-

plification of global warming than those with thicker ice. This finding is in keeping with earlier studies (e.g., references cited in Houghton et al. 2001), which show a prominent role for sea ice in setting the climate sensitivity of the Arctic and even the globe as a whole (Rind et al. 1995). But accurate sea ice simulation is hard to achieve, since ice evolves through complex interactions of mixed-phase saline thermodynamics, radiative transfer, and rheology. Moreover, even a perfect sea ice model will generate errors given a poor simulation of the overlying atmosphere. In particular, the spatial pattern of sea ice thickness is largely determined by surface winds.

While possibly less mysterious than the sea ice, the Arctic surface winds are also poorly understood, and current climate models have difficulty in reliably simu-

---

\* Center for Climatic Research, University of Wisconsin—Madison, Contribution Number 905.

---

*Corresponding author address:* Dr. Eric DeWeaver, Dept. of Atmospheric and Oceanic Sciences, University of Wisconsin—Madison, 1225 West Dayton Avenue, Madison, WI 53706.  
E-mail: deweaver@aos.wisc.edu

lating them. In a study of several simulations from the Atmospheric Model Intercomparison Project (AMIP; Gates 1992), Bitz et al. (2002) found a high bias in wintertime sea level pressure (SLP) off the central Siberian coast, with an accompanying anticyclonic bias in geostrophic surface winds. In an offline sea ice model, they found that the wind bias produced a sea ice pattern with maximum thickness along the Siberian coast, diametrically opposed to the Canadian-side pileup expected from observations. Weatherly et al. (1998) found a high bias in annual-mean SLP over the Beaufort Sea in the National Center for Atmospheric Research (NCAR) Climate System Model (CSM), a precursor to the Community Climate System Model, version 3 (CCSM3) with simpler sea ice dynamics. The associated surface winds forced a sea ice pattern with maximum thickness against the Bering Strait, a 90° rotation from the expected Canadian thickness maximum. A study of an earlier generation of climate models by Walsh and Crane (1992) also found substantial errors in Arctic SLP, with seasonal pattern correlation coefficients between observed and simulated climatological SLP ranging from 0.9 to 0.17.

Previous studies have argued that wind-induced thickness errors derive from errors in the position and strength of the wintertime (December–February; DJF) Beaufort high (Bitz et al. 2002; Weatherly et al. 1998). Yet models also have severe errors in summer surface circulation (Bitz et al. 2002; Briegleb and Bromwich 1998), which could be quite detrimental to sea ice thickness. Some support for a summer influence can be inferred from analysis of observations by Rigor et al. (2002), who found that decadal SLP changes in the summer and winter seasons were accompanied by comparable changes in sea ice motion. They noted that while the summer SLP change is smaller, the internal stress of the ice is also less for the thinner summer ice, so that the ice becomes more sensitive to wind stress as the surface winds slacken. The enhanced sensitivity of the summertime sea ice was also invoked by Serreze et al. (1989), who argued for a 20% reduction in ice concentration in the Canada Basin following extended periods of cyclonic summertime surface winds. The summer sensitivity was quantified by Thorndyke and Colony (1982), who found that, for geostrophic surface winds of the same strength, the response in sea ice motion was stronger in summer than in winter by a ratio of 11 to 8.

Our interest in the seasonality of the surface wind errors comes in large part from our desire to link Arctic surface wind forcing of sea ice to the large-scale general circulation. The wintertime Beaufort high can be regarded as a stationary wave, clearly apparent in plots

of, say, the eddy geopotential height at 1000 and 700 mb (section 5). Attempts to account for the climatological stationary waves usually involve consideration of the strength of the zonal-mean flow, diabatic heating in storm tracks and in the Tropics, vorticity flux by transients, and stationary nonlinear interactions. Held et al. (2002) present evidence that the wintertime stationary waves in high latitudes—including the Beaufort high—depend on the interaction of tropical heating with mid-latitude mountains (their Fig. 11). A better understanding of these dynamics could be helpful in understanding why the Beaufort high is often distorted in GCMs. In contrast to the wintertime circulation, the observed summer circulation of the Arctic is much more zonally symmetric, dominated by a polar low and flanked by the storm track of the Arctic front (e.g., Serreze et al. 2001; Serreze and Barry 1988; Reed and Kunkel 1960). The ability of a model to correctly simulate the wintertime Arctic circulation features may thus be quite independent of its ability to simulate the summertime flow.

Motivated by the difficulty and importance of accurate sea ice simulation, the present study has three goals: 1) to identify the biases in Arctic basin surface winds and sea ice thickness in the NCAR CCSM3, 2) to examine in detail the seasonally varying forcing of the sea ice thickness distribution by the surface winds, and 3) to relate the basin-scale surface wind biases to the large-scale CCSM3 atmospheric circulation. Our examination considers sea ice and circulation differences between two control runs of CCSM3, one at relatively high (T85) resolution and one at a medium (T42) resolution (see section 2 for specifications).

Although neither resolution produces an entirely satisfactory simulation of Arctic sea ice thickness, some improvement is evident at the higher resolution, as discussed in section 3. Are these improvements in sea ice thickness due to genuine improvements in surface winds? If so, what are the most relevant improvements? We examine the surface winds at the two resolutions to address these questions. We also use an offline sea ice model to isolate the mechanical effect of surface winds on the sea ice distribution. In the offline simulations, the surface stress on the top of the ice is calculated either from reanalysis or CCSM3 surface winds, but all other forcings (e.g., air–ice fluxes of latent and sensible heat) are computed from observational datasets (details in section 2c).

The remainder of this paper is divided into six sections. Section 2 discusses the model integrations and reanalysis datasets used in the study, and describes the offline sea ice model that we use to assess the effects of spring and summer surface wind biases on sea ice thick-

ness. Section 3 compares the sea ice and surface winds between reanalysis and the CCSM3 integrations, and section 4 presents the offline sea ice model experiments used to relate the winds to the ice thickness. Section 5 documents the three-dimensional structure of the observed and simulated DJF Beaufort high. This analysis is intended as a first step in understanding how the Beaufort high at the surface is linked to the large-scale circulation of the Northern Hemisphere winter. In section 6, we consider the summertime circulation, and show that, despite the improvement at T85, neither resolution captures the North Polar summer low. Conclusions follow in section 7.

## 2. Data sources and model integrations

### a. Reanalysis data

Reanalysis data for this study come primarily from the National Centers for Environmental Prediction (NCEP)–NCAR reanalysis (Kalnay et al. 1996). Monthly mean wind, height, temperature, and vertical velocity were obtained from the NCEP Web site (currently [www.nomad2.ncep.noaa.gov/ncep\\_data](http://www.nomad2.ncep.noaa.gov/ncep_data)) on 17 pressure levels. These variables are spectrally truncated to T36 by NCEP. In addition to the monthly mean fields, the meridional flux of zonal momentum by submonthly transients was obtained from the same site. For the discussion of low- and bandpass-frequency contributions to the northward momentum flux, daily mean zonal and meridional winds at 200 mb were downloaded from the Web site: [www.cdc.noaa.gov/cdc/reanalysis/reanalysis.shtml](http://www.cdc.noaa.gov/cdc/reanalysis/reanalysis.shtml). Daily means were used for the flux calculations instead of instantaneous values to facilitate comparison with the archived daily data available for the model integrations. Monthly mean surface winds were also obtained from this Web site.

Reanalysis data were also obtained from the European Centre for Medium-Range Weather Forecasting (ECMWF 1997) 40-yr reanalysis (ERA-40). For most fields (e.g., sea level pressure and zonal winds) the two reanalyses agree quite closely (the exception being the vertical motion fields in Fig. 10). ERA-40 data shown here is archived on a  $2.5^\circ \times 2.5^\circ$  latitude–longitude grid.

The period of record for the reanalysis statistics shown here is December 1979 to November 1999. The period was chosen to avoid possible differences in meteorological data relating to the advent of the satellite observations.

### b. CCSM3 integrations

Climate model data used here comes from the NCAR's CCSM3, which consists of atmosphere, land

surface, ocean, and sea ice components that communicate with each other through a flux coupler. Detailed descriptions of the component models and the flux coupler can be found in references in this issue, as well as overviews of the atmospheric and oceanic circulations and global climate (Collins et al. 2006a,b; Dickinson et al. 2006; Holland et al. 2006; Large and Danabasoglu 2006).

We examine two control runs with radiative forcings (e.g., concentration of carbon dioxide) held fixed at 1990 levels during the multicentury integration. The primary difference between the two control runs is a factor of 2 (in each direction) increase in the horizontal resolution of the component atmosphere model, referred to as the Community Atmosphere Model version 3 (CAM3). The higher resolution run is integrated at T85 resolution (triangular spectral truncation at total wavenumber 85), with a  $128 \times 256$  latitude–longitude grid, while the lower is a T42 integration on a  $64 \times 128$  grid. Both resolutions use 26 levels in the vertical, and the resolution of the ocean, land, and sea ice models is the same for both integrations at  $1.125^\circ$  in longitude and  $\sim 0.5^\circ$  in latitude, except in the Tropics where the latitudinal resolution is finer. In addition to the resolution difference, the integrations differ in the tuning of various physical parameterizations (Hack et al. 2006a).

Climatologies of sea ice and atmospheric circulation fields shown here were calculated using years 200 to 219 of the model integrations. The period of record is somewhat arbitrary, but it occurs after large fluctuations during spinup, as described in Collins et al. (2006a). While the period is somewhat short, the key features of the sea ice and circulation are consistent with those of other periods.

### c. The offline sea ice model

The offline sea ice model is an updated version of the one used in Bitz et al. (2002). Specifically the model now includes a subgrid-scale parameterization of the probability density function of ice thickness, known as an ice-thickness distribution model, using the method of Bitz et al. (2001). The physics in the offline model is essentially identical to that in the sea ice component of CCSM3, which uses the same ice-thickness distribution method. However the offline model uses a first-order-accurate numerical solution for horizontal advection with the ice motion field and for the so-called thickness advection of the ice-thickness distribution that results from ice accretion or ablation. Twice as many thickness categories are used in the offline model to compensate for the reduced accuracy of the numerics. The offline model grid is 80-km square Cartesian. Wind stress forcing is calculated from daily mean geostrophic surface

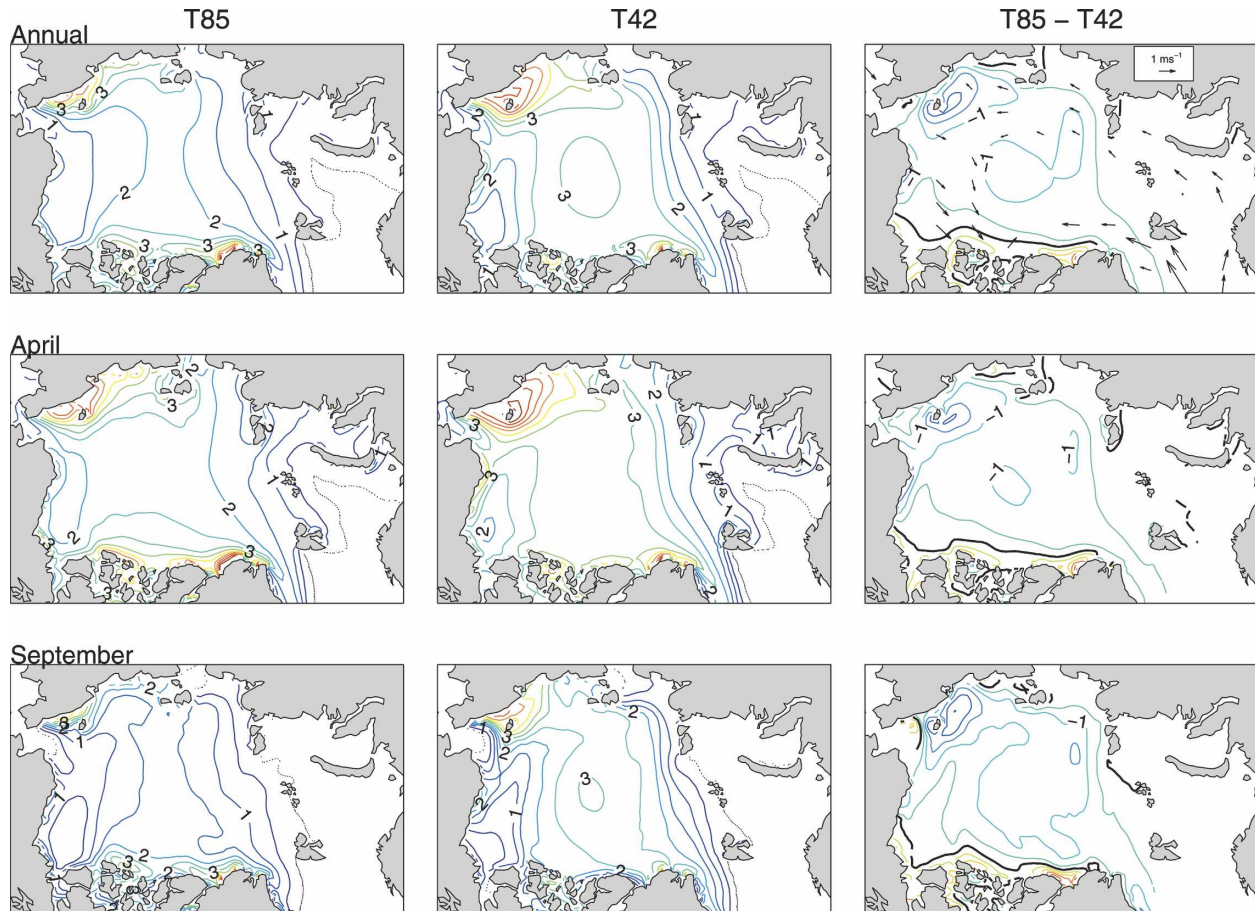


FIG. 1. Climatological sea ice thickness from CCSM3 control runs at (left) T85 and (middle) T42 resolutions, and (right) their difference. (top) Annual-mean, (middle) April, and (bottom) September thickness distributions are shown. Contour interval is 0.5 m, and the thin dotted line is the 3% contour for grid box area covered by ice and indicates the location on of the sea ice margin. The thick black line in the difference plots is the zero contour, and the vectors in the top right panel show the annual-mean wind surface wind difference, with vectors suppressed for wind speeds less than  $0.3 \text{ m s}^{-1}$ . Zero contours are suppressed when less than 3% of the grid box is ice covered.

winds, which are interpolated to the model time step of 3 h. The surface wind stress is computed from the geostrophic wind assuming a constant turning angle of  $25^\circ$  to account for the Ekman boundary layer.

### 3. Sea ice and surface winds

#### a. Sea ice thickness

Figure 1 shows the sea ice thickness climatology for CCSM3 at T85 (left) and T42 (center) resolutions, together with the difference T85–T42 (right; ice thickness is ice volume divided by total grid box area). The annual-mean thickness patterns (top row) show that the ice is generally thicker at the lower resolution, which has a local sea ice maximum in excess of 3 m in the central Arctic, where the T85 sea ice is always less than 2.5 m thick. Substantial differences in the pattern of ice

thickness are also apparent. On the Siberian side, both resolutions have a local thickness maximum on the eastern coastline near Wrangell Island (near the date line), which is much thicker and more extensive in the T42 integration [Yeager et al. (2006) report a similar bias at T31]. There is also a substantial difference in the onshore thickness gradient along the Canadian Archipelago, where ice thickness increases from less than 2.5 m to values locally in excess of 3.5 m near Greenland in the T85 integration. In the T42 case the thickness gradient is less steep near the coast, with no Canadian pileup [a similar pattern was found by Collins et al. (2006a) for CCSM2]. Ice builds up at the northern tip of Greenland in both cases, with a greater buildup at the higher resolution.

To examine the seasonal cycle of the ice thickness, we display in the bottom two rows the thickness pat-

terns for April (middle row), and September (bottom row), the extreme months of the cycle. The patterns at both extremes are similar to the annual mean, with the same preference for more ice on the Canadian coast and less on the eastern Siberian coast at higher resolution. In September the T42 run has a narrow strip of thin ice (less than 2 m thick) along the coast of the Canadian Archipelago (bottom center), while the T85 run has a thickness maximum at the same location (bottom left).

#### *b. Surface winds*

As a first step in relating the thickness pattern to the surface winds, we superimpose the annual-mean T85–T42 surface wind difference on the thickness difference in Fig. 1 (top right). Difference winds generally blow toward higher values of difference thickness near Banks Island. There is also an association between wind shear and thicker ice in the difference fields, especially in the east Siberian Sea (the model is formulated so that wind shear causes the ice to ridge). It is also noteworthy that the difference wind blows into the Arctic from the North Atlantic. This wind difference, together with the thickness difference, leads to a reduction in ice export from the Arctic at T85. M. Holland (2004, personal communication) calculated that the average CCSM3 Fram Strait ice export is in excess of 0.096 Sverdrups (Sv) at T42, while about 0.087 Sv were exported at T85 (her calculation was for years 450–499 of the integration; see also Hack et al. 2006b, Fig. 26). The observed export is estimated to be 0.09 Sv by Vinje (2001).

In Figs. 2 and 3 we examine the surface winds over the Arctic basin for the T85 and T42 simulations and the NCEP–NCAR reanalysis, with the expectation that differences in surface winds can be related to differences in ice thickness. It must, of course, be noted that the ice motion will be slightly to the right of the surface wind (e.g., Hibler and Flato 1992, Fig. 12; Thorndyke and Colony 1982; Serreze et al. 1989; all of whom calculate turning angles from the geostrophic wind rather than the actual wind). Figure 2 shows surface wind vectors for the four seasons at T85 and T42 resolution, together with their difference. These are winds from the lowest model level, at which ambient pressure divided by surface pressure is 0.992 (the model uses a hybrid vertical coordinate which reduces to a standard sigma coordinate at the surface).

Surface winds at the two resolutions have much in common, including northerly flow from the Arctic into the North Atlantic in all seasons, an anticyclonic circulation extending across the basin from the Siberian coast in DJF, and flow from the Canadian Archipelago

to eastern Siberia in September–November (SON). However, there are also significant differences between the two model runs, including differences in the anticyclonic circulation extending outward from the Siberian coast, which is stronger in DJF in the T85 integration but stronger in SON in the T42 simulation. Also, the winds blowing from the Arctic into the North Atlantic are stronger at T42 in all seasons except DJF, a difference that could be consequential for the export of sea ice from the Arctic. A pronounced difference between the runs is the June–August (JJA) polar anticyclone, which is present in the T42 run but absent at T85 [see also Hack et al. (2006a), their Fig. 11, which shows the JJA winds]. The wind difference plots show that in all seasons except DJF the T85 winds have a component toward the Canadian islands relative to the T42 winds. This wind difference is consistent with the thickness patterns in Fig. 1, which show more ice on the Canadian coast for the higher resolution.

Figure 3 compares the T85 surface winds with surface winds from the NCEP–NCAR reanalysis. Reanalysis winds are from the lowest level of the model used to produce the reanalysis, where pressure divided by surface pressure is 0.995. NCEP–NCAR winds are shown for each season in the right column, with the wind difference T85 minus reanalysis in the left column. It is clear from the plot that wind differences between T85 and reanalysis are as strong as the winds themselves. Furthermore, the T85 winds are generally directed more away from the Canadian Arctic and toward eastern Siberia than the reanalysis winds. Comparing this bias with the wind difference in Fig. 2, one can see that the T85 run amounts to a partial correction of the bias in the T42 run, in the sense that the T85 winds are directed more toward the Canadian side than the T42 winds, but still less toward Canada than the reanalysis winds. In the summer (third row), reanalysis winds have a cyclonic circulation around the pole, in striking opposition to the anticyclone in the T42 integration. Thus we can say that that even though the T85 run does not produce the erroneous anticyclone found at T42, it still does not capture the polar cyclone found in reanalysis.

#### **4. Offline sea ice model experiments**

To quantify the effect of the surface wind on the ice we integrate an offline sea ice model, which uses the same ice rheology and thermodynamics as CCSM3 but isolates the influence of the surface winds. Our modeling strategy is to first generate a thickness pattern using winds from the NCEP–NCAR reanalysis, then generate comparable patterns using CCSM3 surface winds at both resolutions. As discussed in section 2c, observa-

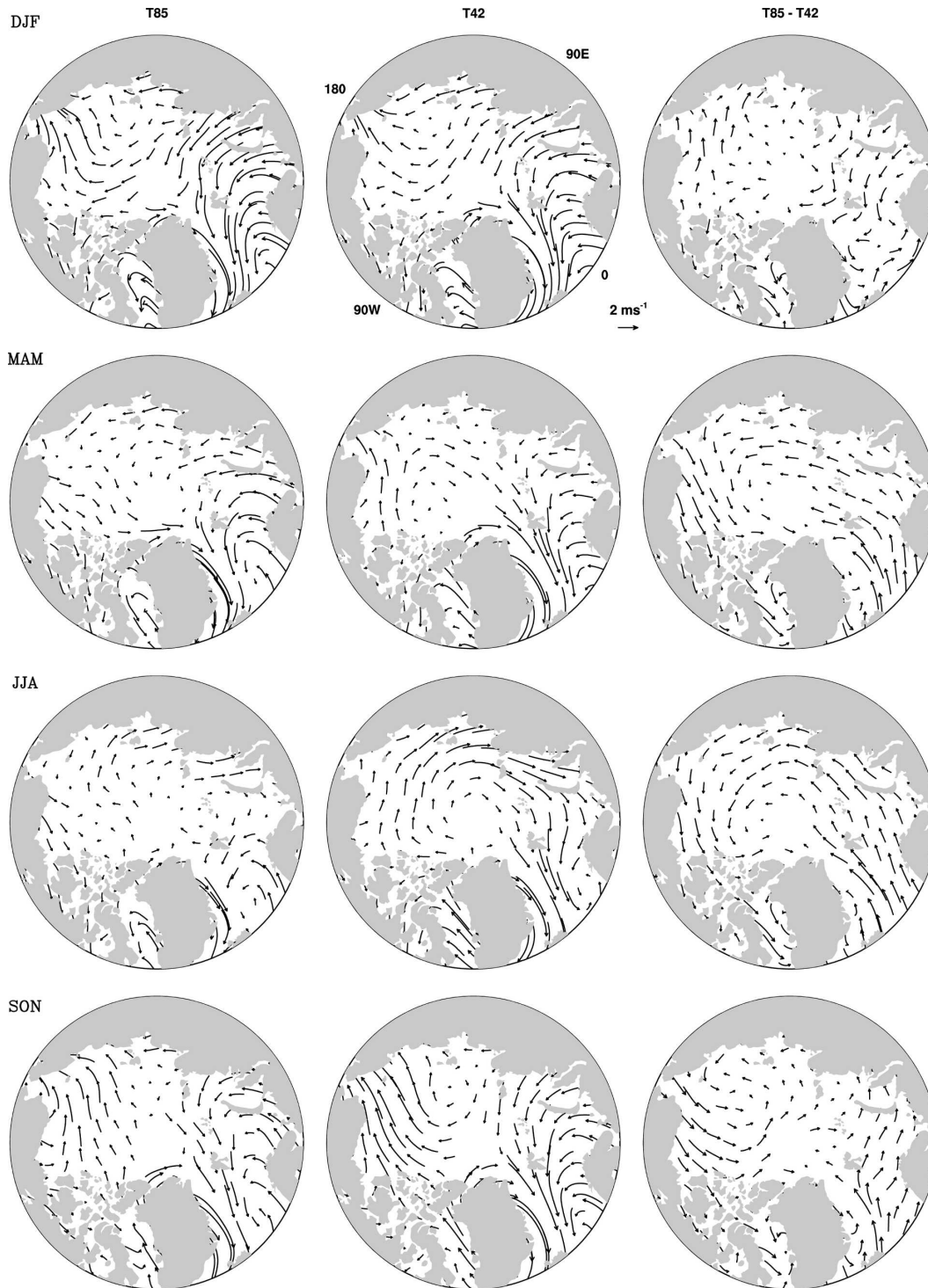


FIG. 2. Climatological winds at the lowest model level for CCSM3 at (left) T85 and (middle) T42, and (right) the difference of T85 and T42 for (top row) winter (DJF), (second row) spring (MAM), (third row) summer (JJA), and (bottom row) fall (SON). Map domain begins at 65°N, and wind vectors are suppressed at the pole. The scale for all vectors is shown in the lower right corner of the top center plot.

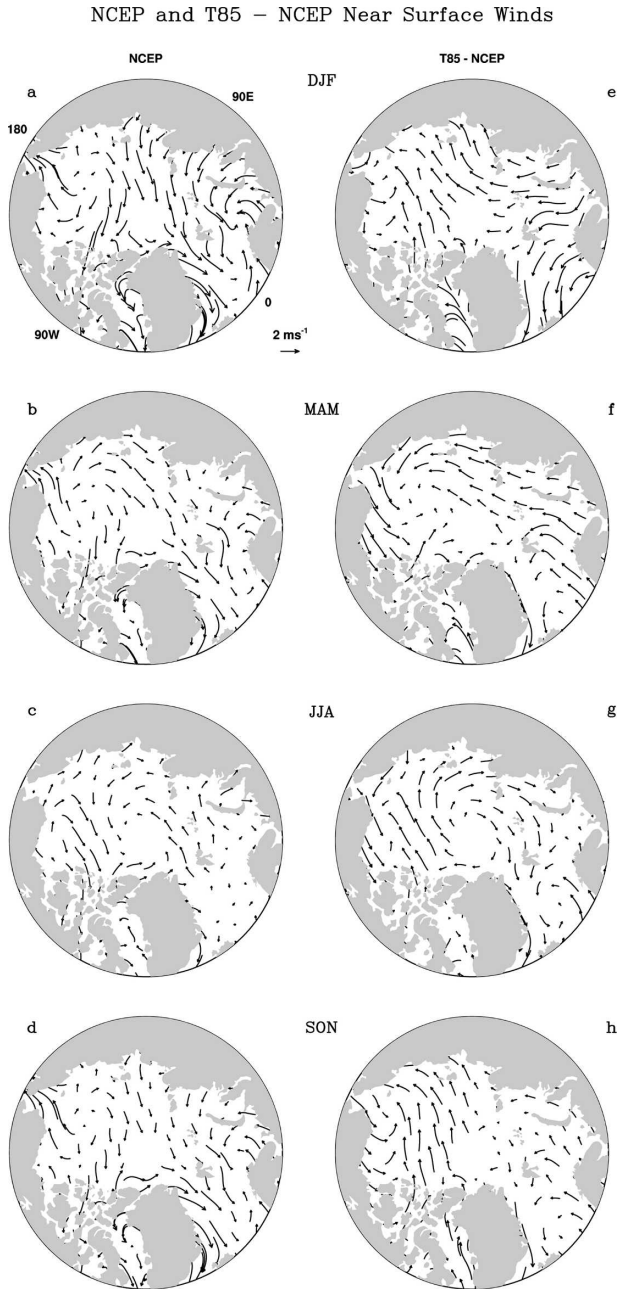


FIG. 3. (left) Climatological surface winds from the NCEP–NCAR reanalysis for (a) winter (DJF), (b) spring (MAM), (c) summer (JJA), and (d) fall (SON). (right) The difference in climatological surface winds between CCSM3 at T85 resolution and NCEP–NCAR reanalysis (CCSM3 minus reanalysis) for (e) winter, (f) spring, (g) summer, and (h) fall. Plotting conventions as in Fig. 2.

tionally derived values are used for all inputs other than the surface wind stress, so that the differences between offline simulations can be ascribed entirely to wind forcing. In addition, only the geostrophic component of the surface winds is used, so simulation differences can

be related to the sea level pressure differences discussed in section 5.

#### a. Offline thickness comparisons

The left column of Fig. 4 shows ice thickness patterns generated by the offline model forced with NCEP/NCAR geostrophic surface winds. The figure shows annual-mean sea ice thickness (top row) together with thickness for April and September (middle and bottom rows), the extreme months of the annual cycle. In all three panels the thickest ice is along the Canadian coastline, with values in excess of 4 m along the whole coast and local maxima in excess of 5 m between Ellsmere Island and Greenland and off the islands of the Canadian Archipelago. Thickness decreases outward across the Arctic basin from the Canadian side, although a second local maximum is apparent in the east Siberian Sea. The annual cycle, assessed by comparison of the middle and bottom panels, is most evident in the cross-basin thickness gradient, as ice thins from April to September along the Siberian and Alaskan coastlines but remains thick on the Canadian coast. The pattern of annual-mean sea ice thickness in the model is similar, although with reduced amplitude, to the pattern Bourke and Garrett (1987) obtained from submarine data. The amplitude difference is partly a matter of definition, as the thickness shown here is ice volume divided by grid box area, while Bourke and Garrett excluded ice-free areas from their mean thickness.

Comparison of the CCSM3 annual-mean patterns in Fig. 1 and the annual-mean NCEP–NCAR pattern in Fig. 4 reveals a substantial discrepancy, as the CCSM3 sea ice does not show the strong preference for thicker Canadian-side ice produced by reanalysis winds. Of the two resolutions, the T85 integration (Fig. 1, top left) is a better match with the offline reanalysis pattern in that it produces a thickness maximum along the Canadian coast, the T42 midbasin maximum is gone, and the Siberian pile up is much reduced. On the other hand, the higher resolution still fails to produce the pronounced cross-basin thickness gradient found in the offline reanalysis calculation.

Offline thickness patterns generated by CCSM3 surface winds are shown in the middle (T85) and right (T42) columns of Fig. 4. In general agreement with the CCSM3 output in Fig. 1, the annual-mean offline thickness patterns are diametrically opposed to the reanalysis pattern (Fig. 4, top left), with thickness increasing across the middle of the basin from the Canadian to the Siberian Arctic. The comparison thus shows that even if all temperature biases in the model were eliminated, the surface wind biases would be sufficient to cause the

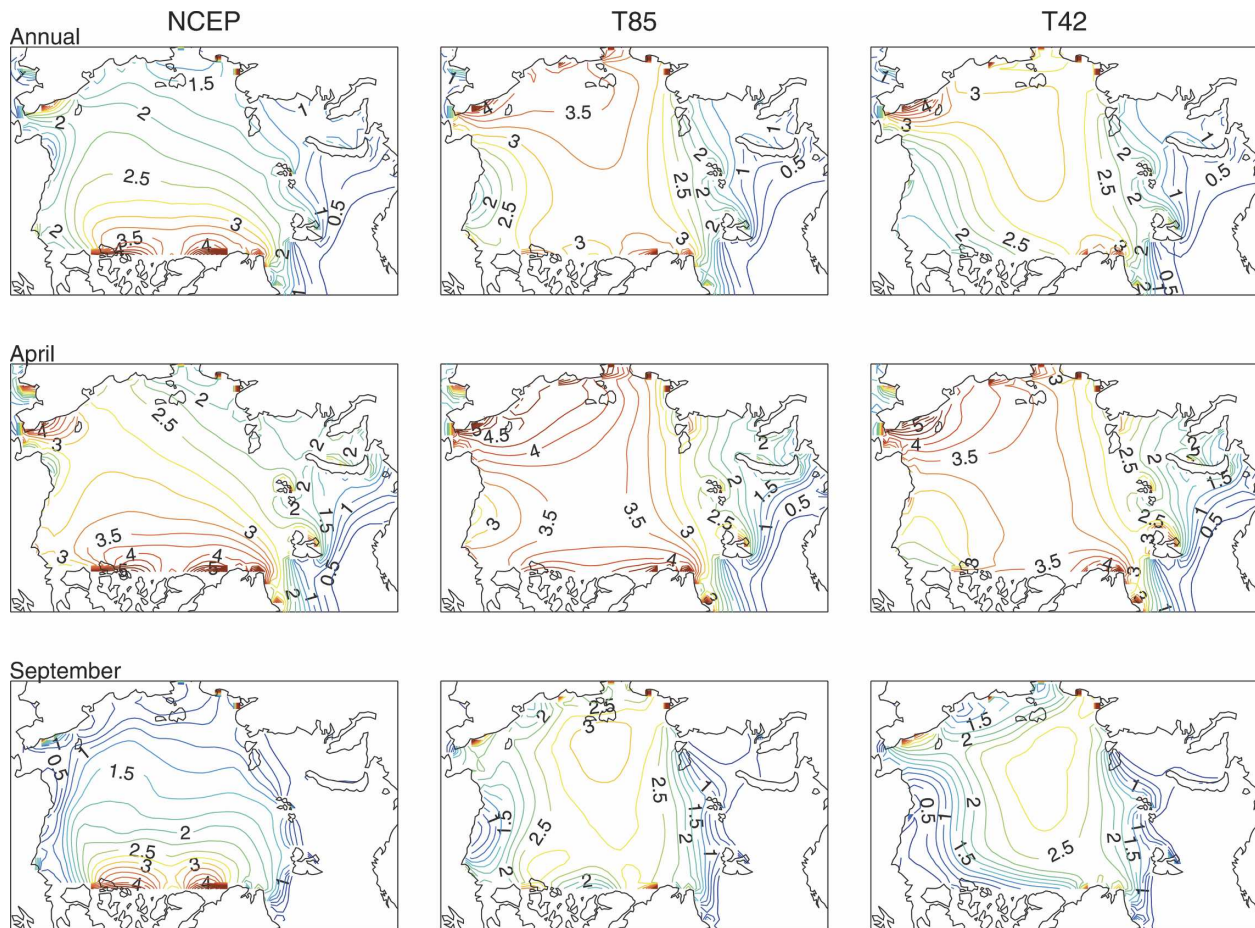


FIG. 4. Simulations from an offline sea ice model forced with surface geostrophic winds from (left) the NCEP-NCAR reanalysis and CCSM3 at (center) T85 and (right) T42 resolution. Annual-mean, April, and September sea ice thickness are shown in the top, middle, and bottom rows, respectively. Contour interval is 0.25 m.

major errors in CCSM3 sea ice. In particular, the reversal of the cross-basin thickness gradient is consistent with the difference winds between CCSM3 and reanalysis (Fig. 3), which are directed toward Siberia in all seasons except March–May (MAM).

Offline sea ice forced by T85 winds is thicker overall, with annual-mean values in excess of 3 m across the basin, or about 0.25 m thicker than ice forced by T42 winds. This difference in overall thickness is in opposition to the thickness difference found in the CCSM3 output (Fig. 1, top row). Differences in mean thickness are usually attributed to thermodynamics (e.g., Randall et al. 1998), so the fact that the 2-m temperature is about 2 K colder at T42 than at T85 (except in summer when temperatures are near the melting point) should be important in promoting more ice growth at the lower resolution. Hack et al. (2006a, their Fig. 2) show further that the entire Arctic troposphere is warmer at T85. However, for the offline calculations, in which atmo-

spheric temperature is the same, the difference must be attributed to nonlinear feedbacks between ice growth and ice motion (e.g., Zhang et al. 2000). Sea ice export from the Arctic is one contributing factor: about 5% more ice (by volume) is exported through Fram Strait (between Greenland and Spitzbergen) in the offline T42 case due to stronger surface winds blowing from the Arctic to the North Atlantic (see Fig. 2).

Additional inspection reveals that the two resolutions differ in the extent of the Siberian pile up, with ice thickness in excess of 3.5 m along the Siberian coast between Wrangell Island and the New Siberia Islands (Novosibirskaya Ostrova, near 145°E) in the offline T85 run. In contrast, thickness forced by the T42 surface winds has a local maximum offshore, with ice about 3 m thick along the coast. The offshore T42 thickness maximum is consistent with the T42 CCSM3 output in Fig. 1. However, the finding of thicker offline ice along the Siberian coast with T85 winds is in opposition

to the CCSM3 output, which shows larger Siberian thickness at the lower resolution. It would be difficult to anticipate the relative extent of the Siberian pile up from the surface winds in Fig. 2. In MAM, JJA, and SON, the T85 winds appear to be more offshore at the eastern end of the Siberian coastline, but significant thickness discrepancies extend further west, where the wind differences tend to be oriented along the coast. In DJF, the T85 surface winds are directed more toward land than the T42 winds along most of the relevant coastline, but this is the season in which the ice should be least responsive to wind stress.

Offline ice thickness differences on the Canadian side are qualitatively consistent with the online differences in Fig. 1, as the T85 surface winds produce thicker ice than their T42 counterparts. In the annual mean, ice thickness decreases westward along the Canadian coast, with values below 2 m extending from the western archipelago to the Alaskan North Slope. In contrast, ice forced by T85 winds has thickness values in excess of 3 m along the entire Canadian archipelago, with a small local maximum along the western side of the archipelago where ice produced by T42 winds is less than 2 m thick. This secondary maximum is consistent with the ice pattern produced by reanalysis winds, although reanalysis winds produce a much stronger maximum. Differences along the Canadian coast are most pronounced in September (Fig. 4, bottom row), when a strong offshore thickness gradient occurs along the Canadian and Alaskan coastlines in the T42-forced simulation.

### *b. Seasonal forcing experiments*

Any attempt to relate biases in ice thickness to biases in surface winds must take into account the strong seasonality present in both. In particular, the preference for thick ice on the Siberian side in the T85- and T42-forced offline simulations is most evident in April (Fig. 4, second row), following the winter season. Thus, although the CCSM3 winds are directed more strongly toward Siberia than the NCEP–NCAR winds in JJA, SON, and DJF, we speculate that the winds of the winter season are more important for establishing the excess Siberian thickness than the summer winds. On the Canadian side, the thinner T42-forced ice is most evident in September (bottom row, left panel), following the summer season. This suggests that resolution-related differences on the Canadian side may be more strongly related to the spring and summer winds. Our interest in the seasonality of wind-forced thickness biases stems from our desire to relate these biases to the large-scale circulation, particularly the strength of the

Beaufort high in winter and the spurious T42 polar anticyclone in summer.

To address the seasonality of the surface winds, we forced the offline model with reanalysis winds for SON and DJF and then switched to CCSM3 wind forcing for MAM and JJA. The integration was performed for each of the CCSM3 resolutions. In both of these seasonal forcing experiments, the departure from the thickness distribution forced by reanalysis winds is due to CCSM3 biases in the spring and summer surface geostrophic winds. An additional pair of seasonal forcing experiments was then performed in which CCSM3 winds were used only in JJA, and reanalysis wind forcing was used in all other months.

The results of these experiments are displayed in Fig. 5 as difference plots between the T85/reanalysis and T42/reanalysis integrations. The top row shows the difference between the T85- and T42-forced integrations in Fig. 4, while the middle row shows the thickness difference between integrations in which the wind forcing for the MAMJJA months is taken alternately from the T85 and T42 CCSM3 output. Consistent with Fig. 4, the top row shows positive thickness differences along the western Canadian and central Siberian coastlines (thicker ice for T85 wind forcing), with larger differences in September (right panel) than in the annual mean (left panel). Comparison of the top and middle rows suggests that virtually all of the Canadian-side differences are due to differences in surface geostrophic wind during spring and summer. The bottom row shows the thickness difference due to JJA wind differences, which accounts for almost half of the Canadian side thickness discrepancy in the top two rows. The contribution of the JJA wind differences to Canadian sea ice differences is even more pronounced in September (bottom right). The comparison thus suggests that the elimination of the erroneous T42 summer anticyclone contributes substantially to the thickening of the sea ice along the Canadian coastline.

## **5. Structure of the Beaufort high**

Attempts to find surface wind–sea ice relationships will inevitably hinge on the subtleties of small-scale wind features, like the onshore component of the flow on opposite sides of the Arctic basin. On the other hand, the quality of atmospheric general circulation model (AGCM) simulations is typically judged by their depiction of large-scale circulation features. Are the relatively small-scale biases in the Arctic surface winds actually manifestations of deficiencies in the large-scale climatological circulation? In fall, winter, and spring, the surface winds of the Arctic Basin are largely deter-

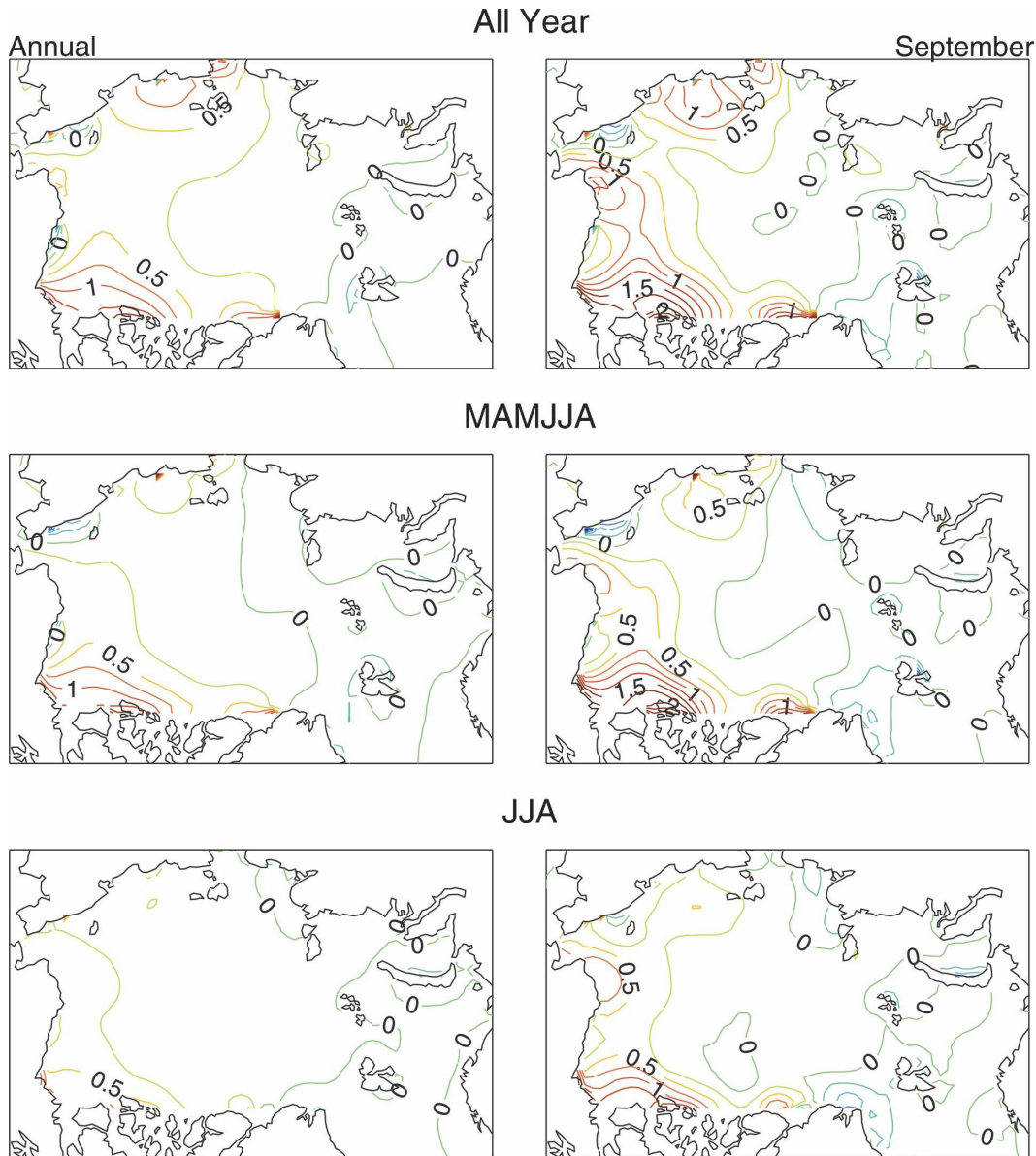


FIG. 5. (top row) (left) Annual-mean and (right) September sea ice thickness difference between offline model simulations forced by CCSM3 T85 and T42 surface winds (T85 minus T42). (middle row) Same as top row, except that the offline simulations are forced with CCSM3 winds from March to August and NCEP-NCAR reanalysis winds from September to February (thickness differences are thus due to the MAM and JJA wind differences in Fig. 2). (bottom row) Same as middle row, except with CCSM3 winds from June to August and reanalysis winds for all other months. Contour interval is 0.25 m.

mined by the location and strength of the Beaufort high and the extension of the Icelandic low into the extreme North Atlantic, while in summer the surface winds circulate cyclonically around the polar low. Thus, we wish to relate the surface circulations in Figs. 2 and 3 to the simulations of these features.

Figure 6 compares the SLP in CCSM3 and the NCEP-NCAR reanalysis in all four seasons. The winter plots (left column) are dominated by the familiar

Aleutian and Icelandic lows and the Siberian and Rocky Mountain highs, all of which are present in the CCSM3 integration, although the simulated oceanic lows are too low and the high over the Rockies is somewhat too strong. Over the Arctic, the DJF Beaufort high appears in the reanalysis (top row) as a ridge that connects the Siberian high with the high over the Rocky Mountains and separates the Aleutian and Icelandic lows. Such a connecting ridge does not appear in the

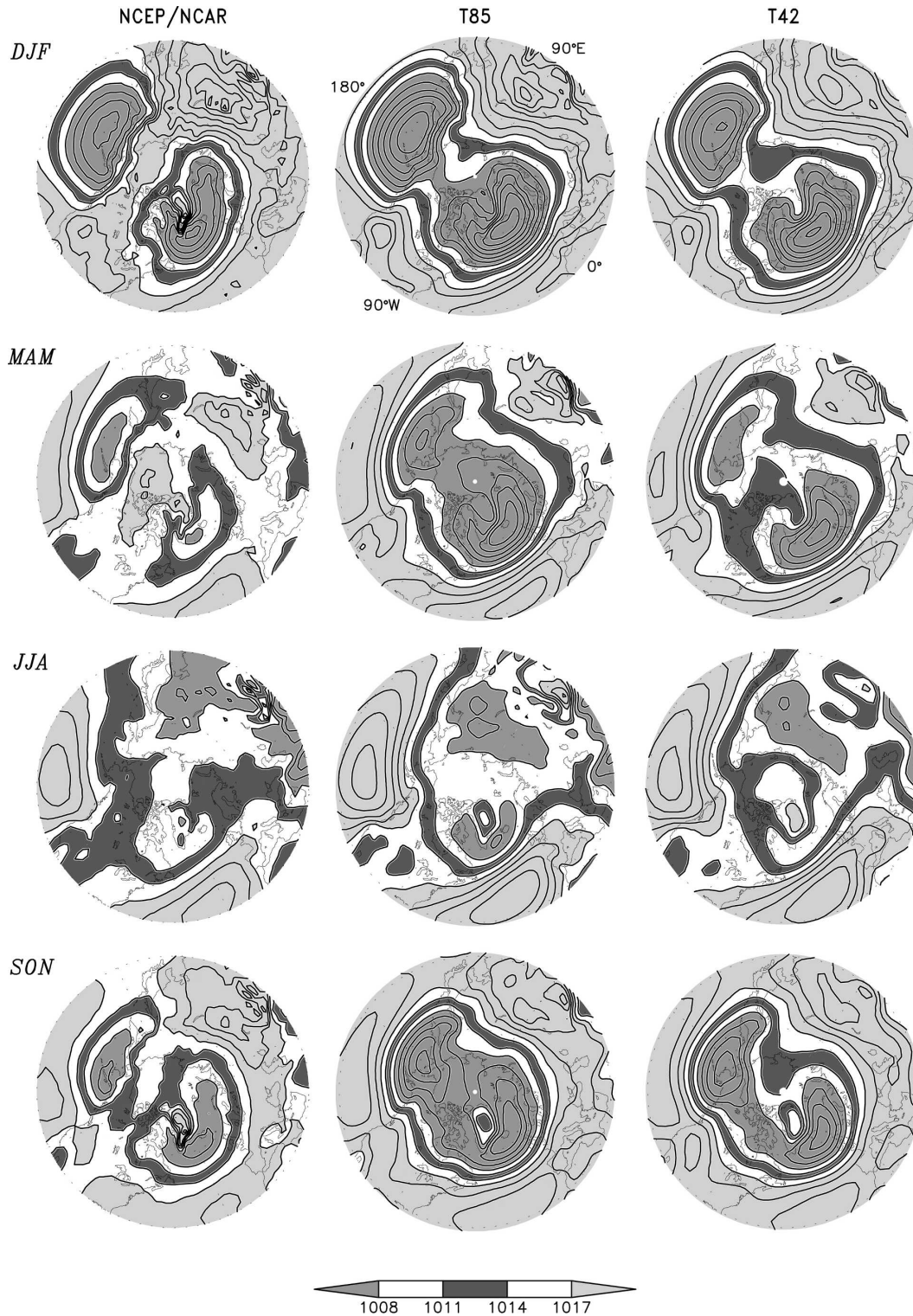


FIG. 6. Climatological SLP from the (left) NCEP–NCAR reanalysis and CCSM3 control runs at (center) T85 and (right) T42 resolutions for (top row) winter (DJF), (second row) spring (MAM), (third row) summer (JJA), and (bottom row) fall (SON). Contour interval is 3 mb, with shading for SLP in excess of 1017 mb, between 1011 and 1014 mb, and less than 1008 mb. Map domain begins at 30°N.

CCSM3 SLP at either resolution. Instead, the oceanic lows connect together across the Arctic basin, while the continental highs are separated by isobars that cross Alaska and eastern Siberia from the Arctic to the North Pacific. The SLP deficit associated with the missing Beaufort high is more pronounced at T85, since at that resolution SLP is lower over the Beaufort Sea. The lower Arctic SLP at higher resolution is accompanied by deeper Aleutian and Icelandic lows than those found in the T42 integration. The deficiency of the simulated Beaufort high is also evident in MAM and SON, as the oceanic lows are too strongly connected in those seasons. The deficiency is most evident in MAM, when in reanalysis the Siberian high diminishes and the Beaufort high emerges as a distinct, independent feature. As in the wintertime simulations, the Icelandic and Aleutian lows are deeper at T85 than at T42 resolution in MAM and SON. Lowering of polar SLP at higher resolution has also been noted in the AGCM of the Geophysical Fluid Dynamics Laboratory (S. Klein 2004, personal communication), and in earlier studies (e.g., Boville 1991).

The consequences of the SLP biases for surface winds can be appreciated by comparing Fig. 6 with Figs. 2 and 3. The wintertime Beaufort ridge in reanalysis is accompanied by geostrophic surface flow that crosses the Arctic basin from Siberia to Canada (Fig. 3a). In the absence of the ridge, this cross-basin flow does not occur in the model, which instead produces a surface flow that leaves the Siberian coast near 90°E and returns to land near Wrangell Island on the eastern Siberian coast (Fig. 2, top left and center). The surface wind bias toward the Siberian coast in the T85 simulation (Fig. 3e) can thus be interpreted as a consequence of the weakness of the Beaufort high. The same analysis applies at both resolutions for SON, and for the T85 integration in MAM.

The Beaufort high is a surface feature by definition, but we expect it to have a close association with the overlying atmosphere, which could provide insights into the dynamics of the surface high. For example, the extreme cold surface temperatures of Siberia and central Asia are usually invoked in explanations of the Siberian high (e.g., Ramage 1971, section 3.1). This association is borne out by the baroclinic cold core vertical structure of the high. In addition, the anticyclonic surface winds circulating around the high must be maintained against friction by convergence of anticyclonic vorticity above the high, most of which occurs in the upper troposphere. As a tentative first step in understanding the dynamics of the surface high, we wish to identify the vertical structure of the flow associated with it, and determine whether the flow is best de-

scribed as barotropic or baroclinic. Our variable of choice for this task is the eddy geopotential height (departure of geopotential height from its zonal average), plotted in conjunction with the eddy temperature field, from reanalysis data and CCSM3 output.

DJF eddy geopotential height for the Northern Hemisphere extratropics is plotted in Fig. 7 for the NCEP–NCAR reanalysis. The 1000-mb plot (Fig. 7a) shows that the most prominent SLP features—the oceanic lows and continental highs—are well described by eddy height, as is the Beaufort high. These features are also present at 700 mb (Fig. 7b), but with the expected differences: the Aleutian and Icelandic lows are shifted westward, and the Siberian high is much reduced, consistent with its expected cold-core structure (e.g., Nigam and DeWeaver 2003). For our purposes, the most noteworthy feature is the Beaufort high, which appears at 700 mb as a closed isobar, separated from the Siberian high but with some connection to the high over the Rockies. While the Siberian high diminishes from 1000 to 700 mb and the Rocky Mountain high amplifies through the same layer, the Beaufort high has the same amplitude at both levels.

The vertical structure of the Beaufort high is further examined in Fig. 7c, a zonal–vertical cross section of the eddy height at 75°N in which the Beaufort high is found at and slightly to the east of the date line. In addition to the height contours, the figure shows the eddy temperature field at that latitude. In agreement with the 1000- and 700-mb plots the figure confirms the barotropic structure of the high, which has some amplification in the upper troposphere/lower stratosphere and an additional intensification in the boundary layer, where eddy temperatures are coldest. It is clear from the figure that, unlike the Siberian high, the Beaufort high is not closely associated with cold lower tropospheric temperatures, although the figure leaves open the possibility that the time-mean high can be viewed as a “graveyard of anticyclones” (e.g., Serreze and Barry 1988).

Eddy height from the CCSM3 integrations is shown in Fig. 8, with horizontal plots at 1000 mb in Figs. 8a (for T85) and 8b (for T42). An advantage of eddy height as a marker for the surface highs and lows is that subtracting the zonal mean factors out the general tendency for lower pressure at the higher resolution. As with SLP in Fig. 6, comparison of eddy height in Figs. 7 and 8 shows that the Beaufort high is much weaker in the model than in the reanalysis. The vertical structure of the eddy height and temperature at 75°N is shown in Figs. 8c and 8d for the T85 and T42 resolutions, respectively. These panels show that the 1000-mb highs at both resolutions are associated with the coldest lower tropospheric temperatures at that latitude, between

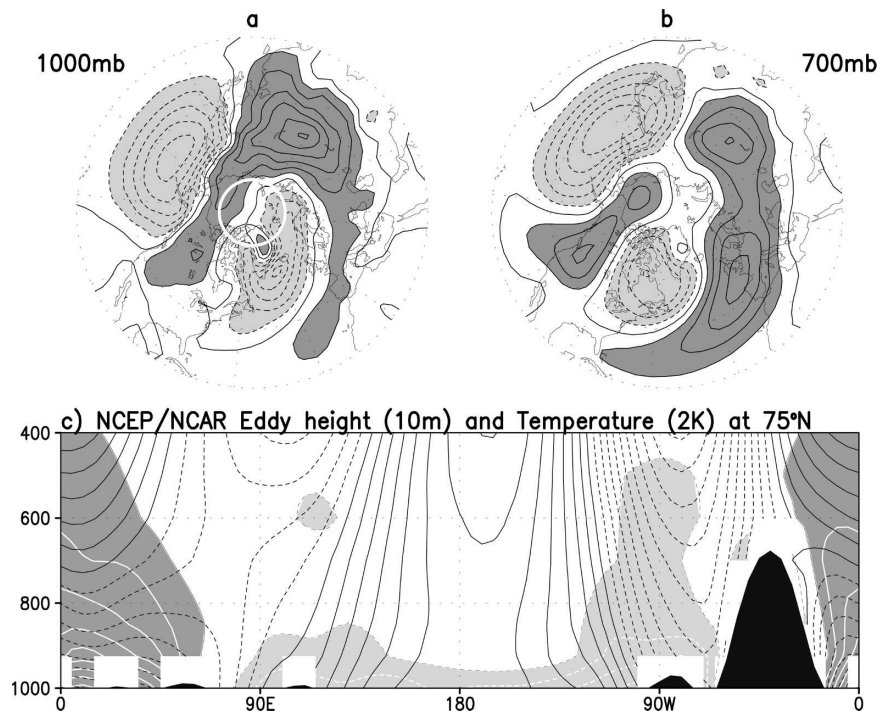


FIG. 7. DJF eddy geopotential height at (a) 1000 and (b) 700 mb from the NCEP–NCAR reanalysis. Contour interval in both panels is 25 m, with dark (light) shading for positive (negative) values in excess of 25 m; (c) 1000–100-mb zonal–vertical cross sections of eddy geopotential height and eddy temperature at 75°N for NCEP–NCAR reanalysis. Contour interval for eddy height in (c) is 10 m, and eddy temperature is plotted in 2-K contours, with dark (light) shading for positive (negative) values in excess of 2 K, and zero contours suppressed. The white space circle in (a) shows the 75°N latitude circle. Dashed contours denote negative values in all panels.

90°E and the date line. In the T42 case the cold temperatures extend upward to 400 mb and are associated with a strong upper-level trough that is much weaker in the higher resolution (in examining this figure it should be noted that  $T \propto -p\partial\phi/\partial p$ , so for a given temperature perturbation the vertical spacing of the height contours will be closer at lower pressure). The collocation of the upper trough and the surface high demonstrate a clear cold-core structure, which, though appropriate for the Siberian high, is not correct for the Beaufort high. There is, however, an upper-level ridge east of the date line that is reminiscent of the upper part of the Beaufort high in Fig. 8c, so one could claim that the model is able to simulate the upper-level eddy height associated with the surface Beaufort high.

## 6. Maintenance of the zonal-mean summer circulation: The Arctic Ferrel cell

The summer circulation deserves separate treatment for two reasons. First, summer is the only season when the circulation cannot be easily described in terms of

the Beaufort high and the oceanic lows. In the absence of strong zonal asymmetries, the structure and dynamics of the summertime flow can be conveniently portrayed through zonal averages of the relevant dynamical variables. Second, the summer surface circulation at T42 is in strong opposition to the reanalysis circulation, with a polar anticyclone instead of a cyclone. In this section we examine the underlying dynamics of the anticyclonic bias and the reasons for its reduction in the T85 integration.

Figure 9 shows the JJA zonal-mean SLP and surface zonal wind  $[\bar{u}_s]$ , where the overbar and brackets represent averaging in time and longitude, respectively. The difference in JJA polar SLP between the T42 (represented dotted lines in all panels) and T85 (the dashed lines) integrations is evident in Fig. 9a in which the T42 SLP has a maximum value of about 1016 mb, comparable to midlatitude SLP values, while T85 SLP is close to 1010 mb. Polar SLP from NCEP–NCAR reanalysis (Fig. 9b, solid line) is near 1009 mb, so there is a clear improvement in SLP at the higher resolution. The

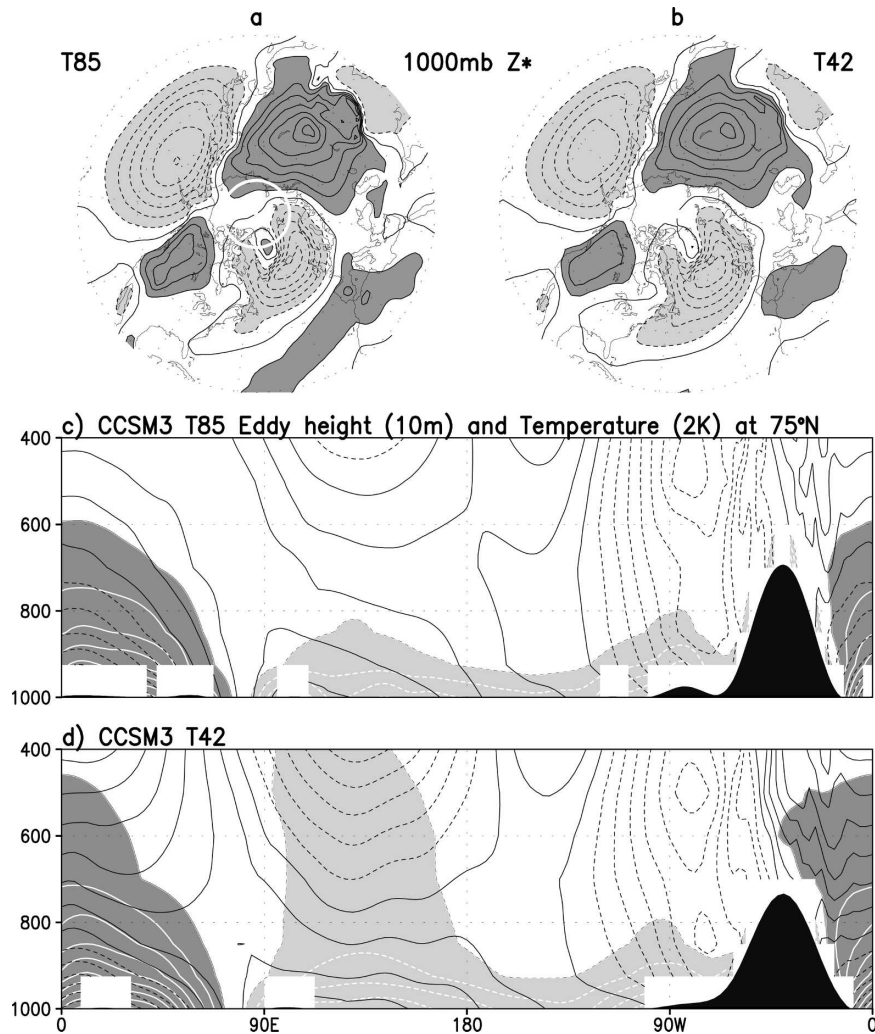


FIG. 8. DJF eddy geopotential height at 1000 mb for CCSM3 at (a) T85 and (b) T42 resolution, and 1000–100-mb zonal–vertical cross sections of eddy geopotential height and eddy temperature at 75°N for (c) T85 and (d) T42 integrations. Contours and shading as in the previous figure.

dashed–dotted line in Fig. 9b represents zonal-mean SLP from the ERA-40 reanalysis, which agrees closely with the NCEP–NCAR profile. In both reanalyses, SLP has a qualitatively different structure than CCSM3, since reanalysis SLP has a local maximum at 70°N and a minimum at the pole.

The geostrophic consequence of the polar minimum is that reanalysis  $[\bar{u}_s]$  is westerly north of 70°N, with a maximum just above  $1 \text{ m s}^{-1}$ , comparable to the strength of the midlatitude westerlies. In contrast, the T42  $[\bar{u}_s]$  is easterly for all latitudes north of about 65°N, reminiscent of the polar easterlies of the standard three-cell general circulation model (e.g., Palmén and Newton 1969, Figs. 1.2 and 4.1). T85  $[\bar{u}_s]$  is a partial correction of the T42 easterly bias, with weaker polar

easterlies than T42 and weak westerlies between 80° and 85°N. A strong bias in CCSM3  $[\bar{u}_s]$  also appears in the midlatitudes, where at both resolutions the simulated surface westerlies reach a maximum of  $3 \text{ m s}^{-1}$ , about twice the maximum in reanalysis. A bias toward strong surface westerlies, including Southern Hemisphere westerlies, has also been noted by Large and Danabasoglu (2006), Yeager et al. (2006), and Hurrell et al. (2006; their results are for CAM3 AMIP integrations).

We next consider the mean meridional circulation ( $[\bar{v}]$ ,  $[\bar{\omega}]$ ) accompanying the zonal-mean SLP profiles. Ekman balance requires that the cyclonic winds around a polar low have a poleward ageostrophic component, with rising motion over the pole to satisfy mass conti-

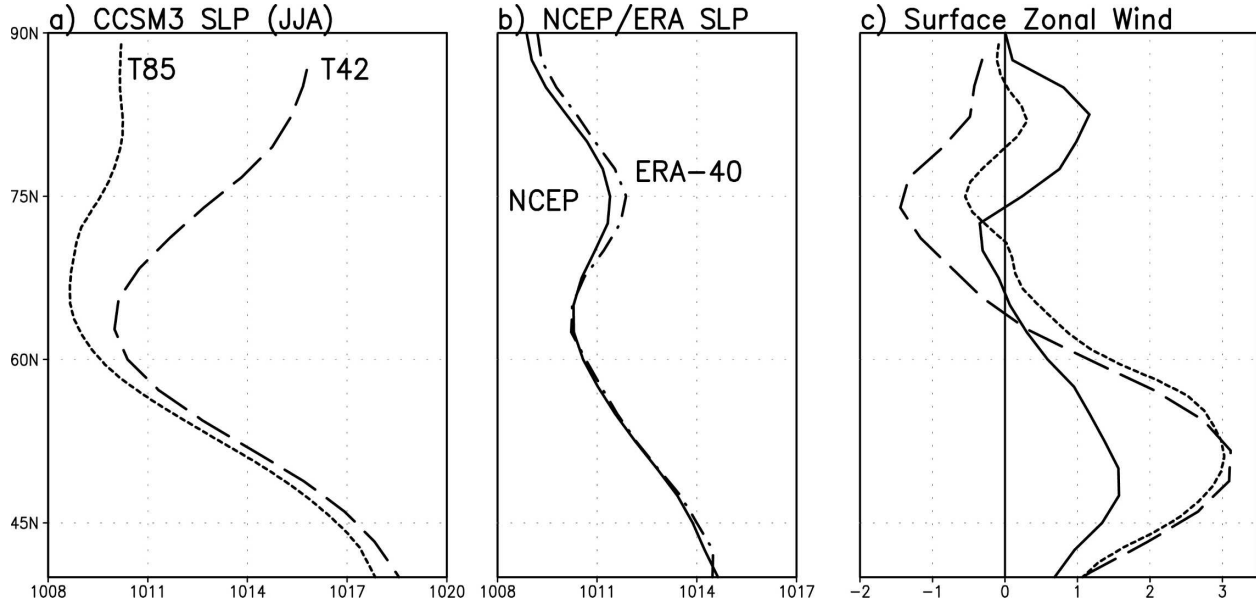


FIG. 9. JJA zonally averaged SLP for CCSM3 at (a) T85 and T42 resolution, and (b) for the NCEP-NCAR and ERA-40 reanalyses, and (c) zonally averaged surface zonal wind for the T42 and T85 CCSM3 integrations and the NCEP-NCAR reanalyses. In all panels, dotted (dashed) curves represent the T85 and T42 integrations, and solid lines are used for the NCEP-NCAR reanalysis. In (b) the dashed-dotted line shows the ERA-40 reanalysis.

nunity. The overturning motion for a model with a polar SLP maximum would be in the opposite direction. These expectations are confirmed in Fig. 10, in which streamlines are used to show the sense of the Eulerian-mean meridional circulation in Figs. 10a–d, and  $[\bar{\omega}]$  is shown in Figs. 10e–h.

The sense of the meridional–vertical circulation for the two reanalyses (Figs. 10a,b) is similar, with the summer Hadley cell extending from about 15°N to the northern midlatitudes, and a Ferrel cell with rising motion around 60°N and subsidence below and to the south of the jet core (isotachs of  $[\bar{u}]$  are shown in Figs. 10a–d). Poleward of 60° the standard three-cell general circulation model has a single thermally direct polar cell, but here we find two cells: a thermally direct cell with subsidence near 75°N (the latitude of the SLP maximum in Fig. 9b) and a thermally indirect cell with rising motion at the pole. The strength and extent of the polar rising motion differs substantially between NCEP-NCAR and ERA-40, with much stronger NCEP-NCAR  $[\bar{\omega}]$  values.

The CCSM3 mean meridional circulation (Figs. 10c,d) has Hadley and Ferrel cells in essentially the same locations as the reanalysis, but north of 60° we find a single thermally direct polar cell with subsidence at high latitudes. In Fig. 10g the T85  $[\bar{\omega}]$  has a nodal line very near the pole, indicating that rising motion has been curtailed at the pole in association with the elimination of the polar anticyclone (Fig. 9a). However, nei-

ther resolution produces the polar Ferrel cell found in reanalysis.

A further difference between reanalysis and CCSM3 zonal-mean circulations is the poleward lobe of the upper-tropospheric jet found above the latitudes of subpolar descent (around 75°N) in reanalysis. The existence of an Arctic westerly jet, distinct from the midlatitude jet, has been documented by Serreze et al. (2001), who showed cross sections through the jet at several longitudes and associated it with the Arctic frontal zone. Of course, the dynamical relationship between the mean meridional circulation and the structure of the upper-level jets is somewhat indirect, and jet structure cannot be inferred from the mean meridional circulation or vice versa. Nevertheless it is noteworthy that without the polar Ferrel cell CCSM3 does not produce the poleward lobe at either resolution.

We have seen that in reanalysis the zonal-mean surface westerlies are almost as strong in the Arctic as they are in midlatitudes, and the T42 Arctic easterlies are comparable in strength to the reanalysis Arctic westerlies (Fig. 9c). Since the surface stress associated with these westerlies constitutes a zonal momentum sink for the atmospheric column, convergence of zonal momentum flux is required to maintain the westerlies. Thus the surface wind differences in Fig. 9c suggest large differences in zonally averaged zonal momentum flux between reanalysis and the CCSM3 simulations.

These differences are examined in Fig. 11, starting in

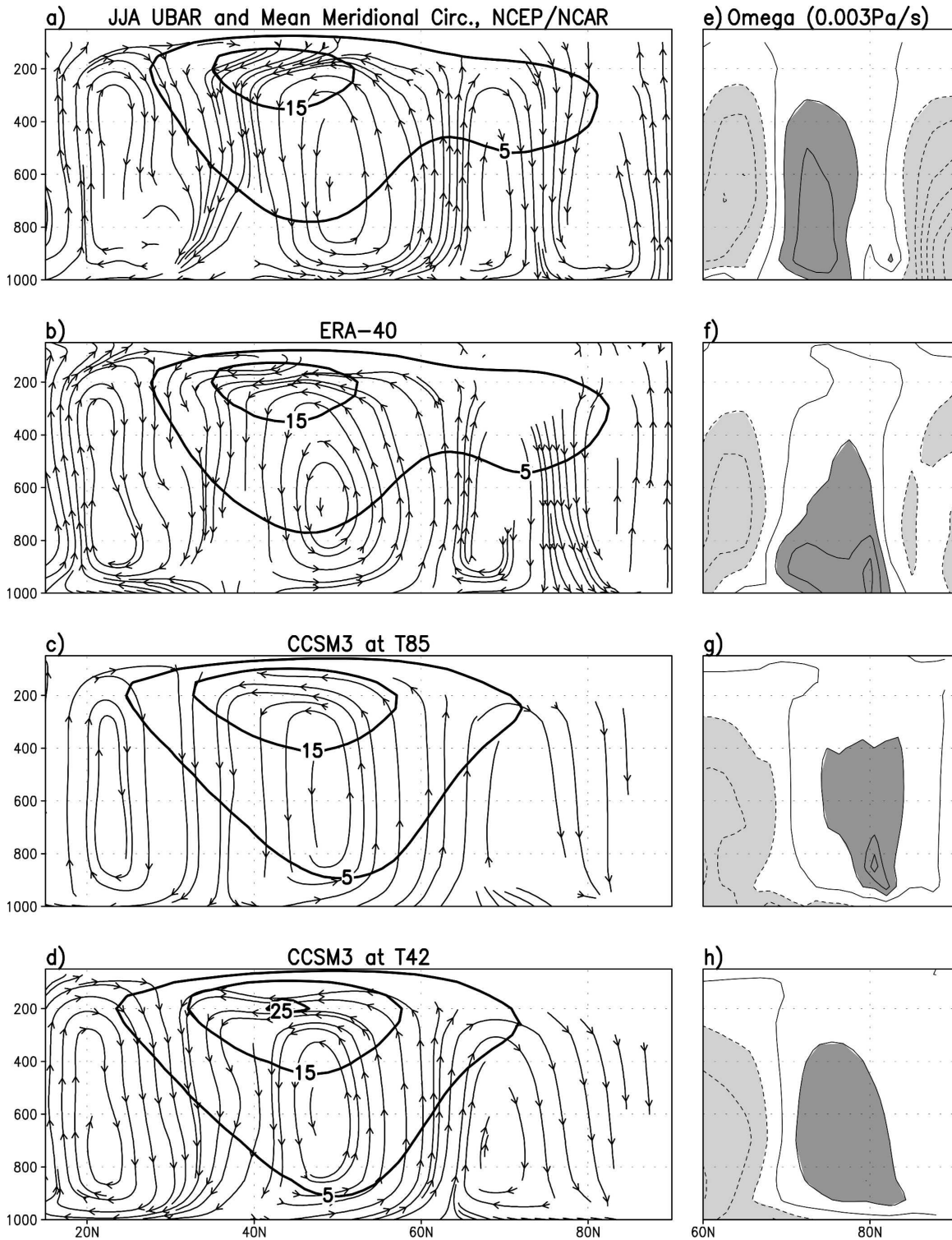


FIG. 10. JJA mean meridional circulation  $[\bar{v}, \bar{w}]$  and mean zonal wind  $[\bar{u}]$  for the (a) NCEP-NCAR and (b) ERA-40 reanalyses, and CCSM3 at (c) T85 and (d) T42 resolutions. (right) Pressure vertical velocity  $[\bar{\omega}]$  from (e) NCEP-NCAR and (f) ERA-40 reanalyses, and (g) T85 and (h) T42 integrations;  $[\bar{u}]$  in (a)–(d) is plotted with 5, 15, and 25  $\text{m s}^{-1}$  contours. The contour interval in (e)–(h) is 0.003  $\text{Pa s}^{-1}$ , with dark (light) shading for positive (negative) values in excess of 0.003  $\text{Pa s}^{-1}$ . The z-coordinate vertical motion for the streamlines in (a)–(d) was calculated hydrostatically from  $[\bar{\omega}]$  and multiplied by 350 to produce streamlines with comparable meridional and vertical spacing.

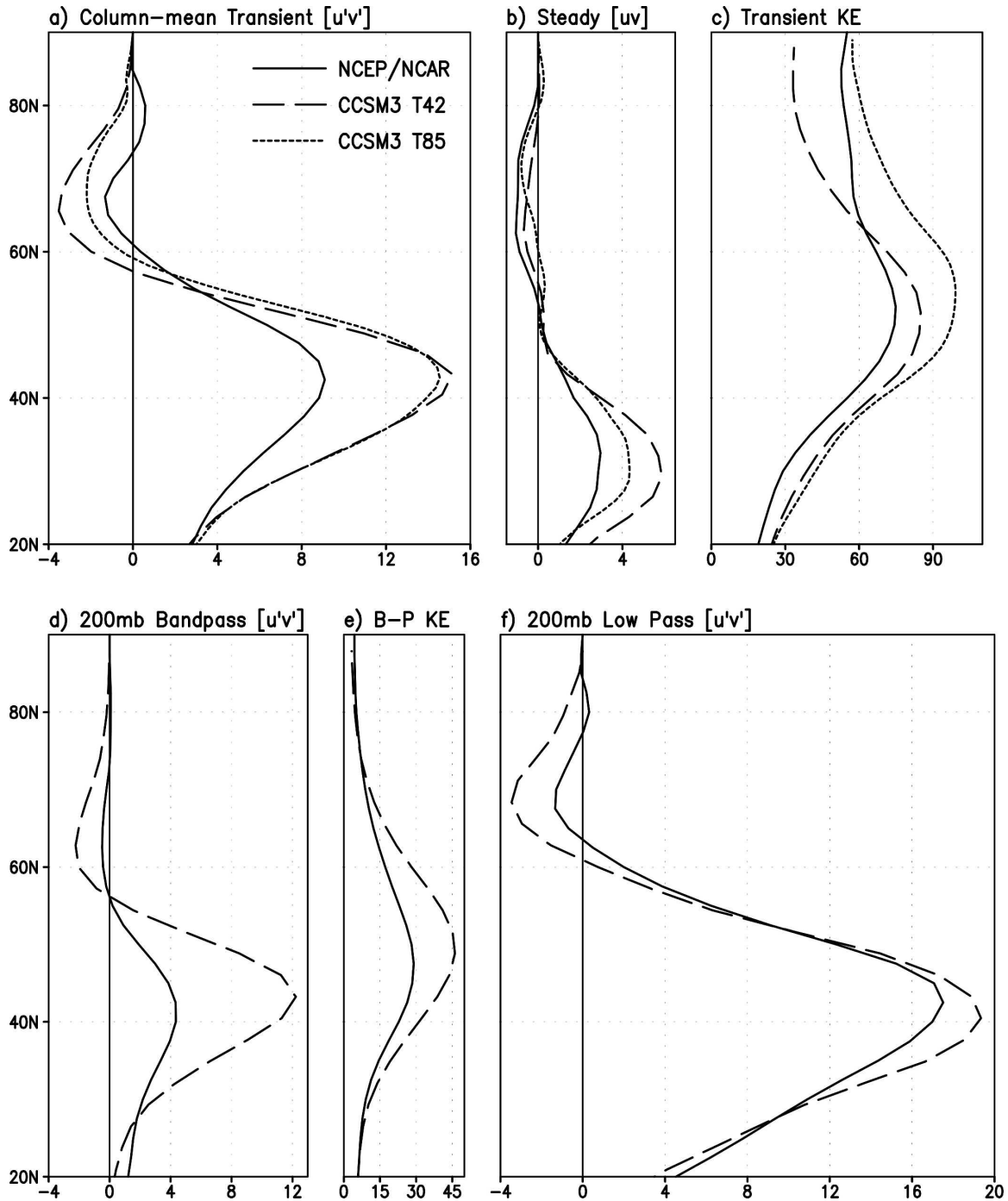


FIG. 11. JJA column-mean meridional flux of zonal momentum from the NCEP–NCAR reanalysis and CCSM3 by (a) submonthly transients and (b) the time-mean JJA flow, as described in section 6. (c) JJA column-mean submonthly transient kinetic energy from NCEP–NCAR reanalysis and CCSM3; (d) 200-mb momentum flux by bandpass-filtered transients with time scales of  $\sim 2$ –6 days (see section 6 for details). (e) Kinetic energy of transients used in (d); (f) 200-mb momentum flux by low-pass-filtered transients with time scales greater than 10 days. In all panels, solid lines show the reanalysis, dashed lines show the T42 integration, and dotted lines depict the T85 integration. Units are  $\text{m}^2 \text{s}^{-2}$ .

Fig. 11a with the zonally averaged meridional flux of zonal momentum by transients  $[u'v']$ , in which  $u'$  and  $v'$  are departures from the June–July–August monthly means of  $u$  and  $v$  averaged over the 20 yr of record (for CCSM3 we used the average of the archived monthly mean flux  $\overline{uv}^m$  for each month, minus the steady flux  $\overline{u^m v^m}$  for that month, where  $(\overline{\quad})^m$  represents a monthly mean). The zonally and vertically averaged zonal momentum flux by the steady climatological  $u$  and  $v$ , including zonal-mean and zonally asymmetric winds, is shown in Fig. 11b (the pressure-weighted vertical average is from the surface to 100 kPa). In accord with the mean-meridional circulation in Fig. 10, the reanalysis transient momentum flux is poleward at high latitudes (from about 75° to 85°N), while the CCSM3 momentum flux is equatorward for all latitudes north of about 60°N. It is evident from Fig. 11a that, in addition to the opposite direction of the high latitude fluxes, the meridional flux of zonal momentum is considerably stronger in CCSM3 than in reanalysis. In the midlatitudes, just north of 40°, CCSM3 momentum flux is about 60% stronger, and in the region around 65°N where reanalysis and CCSM3 fluxes are both equatorward the CCSM3 flux is about twice as strong. CCSM3 momentum flux by the steady (Fig. 11b) flow is also stronger near 30°N, but in high latitudes the T85 steady momentum flux agrees closely with NCEP–NCAR flux. Finally, we note that while momentum fluxes from the T85 and T42 integrations are in close agreement in midlatitudes, there is a reduction of polar cap momentum flux in the T85 integration. This reduction is in general agreement with the reduction of the polar easterlies at T85.

Larger eddy momentum fluxes can be generated either by stronger eddy amplitudes or by a greater correlation between  $u'$  and  $v'$ . In Fig. 11c we address the question of eddy amplitude by plotting the zonally and vertically averaged kinetic energy  $[(u'^2 + v'^2)/2]$  for the submonthly transients from Fig. 11a. According to Fig. 11c, midlatitude transient kinetic energy (TKE) is stronger in CCSM3 than in reanalysis by about 15% at T42 (larger values at T85), but this is a small excess compared to the difference in momentum flux. North of 60°N the reanalysis TKE remains close to  $60 \text{ m}^2 \text{ s}^{-2}$ , but the CCSM3 TKE decreases toward the pole. A strong high-latitude difference is evident between the two resolutions, since the T42 polar TKE is only half of the reanalysis value ( $30 \text{ m}^2 \text{ s}^{-2}$  versus  $60 \text{ m}^2 \text{ s}^{-2}$ ) while T85 TKE (dotted line) is roughly the same as in reanalysis. The difference in TKE is the opposite of the flux difference, since the lower resolution has stronger momentum flux in spite of the reduced TKE. Evidently the  $(u', v')$  correlation (the meridional tilt of the eddies)

is reduced as the eddies become stronger at higher resolution.

In Figs. 11d–f we further examine the eddies using bandpass- and low-pass filtered winds from reanalysis and the T42 CCSM3 run at 200 mb, the upper-tropospheric level at which daily mean data were archived for CCSM3. Transient winds  $u'$  and  $v'$  were generated by removing the first 12 harmonics of the annual cycle from the daily data, after which the transients were filtered using bandpass and low-pass filters given in von Storch and Zwiers (2001, columns 5 and 4, of their Table 17.1), which retain synoptic and low-frequency time scales (roughly 2–6 days and longer than about 10 days). Zonal means of  $u'$  and  $v'$  were retained, but no significant differences were found when the fluxes were computed using only the zonally asymmetric components of  $u'$  and  $v'$  (i.e., the wave momentum flux is dominant).

Consistent with the submonthly fluxes in Fig. 11a, the synoptic momentum flux in Fig. 11d is stronger for the model than for reanalysis, only in this case the difference is much larger—up to 3 times larger for the midlatitudes. This difference is only partly due to stronger eddies, since the bandpass-filtered TKE (Fig. 11e) is about 50% stronger for the model than for the reanalysis ( $45 \text{ m}^2 \text{ s}^{-2}$  for the T42 run,  $30 \text{ m}^2 \text{ s}^{-2}$  for reanalysis). The stronger synoptic fluxes are thus partly the result of a greater correlation between  $u'$  and  $v'$ , that is, a stronger southwest to northeast tilt of the eddies.

North of 60°N, the southward synoptic momentum flux is considerably larger for the model while the eddy kinetic energies are more comparable, implying a stronger northwest–southeast eddy tilt for CCSM3. In these latitudes, the synoptic contribution to zonal momentum flux is smaller than the contribution of the low-pass eddies (Figs. 11d, f), consistent with the idea that waves with smaller phase speeds can propagate farther into latitudes of weak westerlies (e.g., Randell and Held 1991). In midlatitudes, the low-pass eddy momentum flux is in favorable agreement between CCSM3 and reanalysis, unlike the synoptic flux. But in high latitudes (between 60° and 80°N) the southward flux of zonal momentum by low-pass eddies is stronger in CCSM3 by a factor of 2. Thus both synoptic and low-pass momentum fluxes contribute to the maintenance of the spurious Arctic surface anticyclone in the T42 CCSM3 integration.

A more thorough investigation would be required to clarify the relationship between the excessive momentum flux and the summer polar anticyclone. It would of course be difficult for the model to maintain a westerly Arctic surface circulation in the face of transients that export westerly momentum from the polar cap. Also,

the midlatitude  $[\overline{u'v}']$  differences in Fig. 11a suggest that the momentum flux bias is a bias of the general circulation rather than an Arctic phenomenon. Excess transient momentum fluxes are also found in the winter season and in the Southern Hemisphere, accompanied by strong surface zonal winds [not shown, but see Hurrell et al.'s (2006) discussion of CAM3 biases]. Presumably the momentum flux biases in all seasons and regions have similar dynamical origins. On the other hand, the T85 run has the same excess northward momentum flux in midlatitudes, but weaker easterly momentum flux in the polar cap. This suggests that the midlatitude and polar cap momentum fluxes may be somewhat independent of each other. The reasons for an exclusively polar improvement at higher resolution are not clear at present.

## 7. Summary and conclusions

Our examination of Arctic sea ice and atmospheric circulation consists of two parts. First, we seek to relate the spatial pattern of sea ice thickness to the seasonally varying surface winds, and account for CCSM3 thickness biases in terms of resolution-dependent surface wind biases. To isolate the effect of wind forcing we use an offline sea ice model, in which winds are specified from either reanalysis or model simulations, but all other inputs are prescribed from observational data. The offline model is used to generate an observationally derived thickness pattern, which can then be compared with thickness patterns generated in the course of CCSM3 integrations, as well as patterns generated by forcing the offline model with CCSM3 surface winds. Based on these comparisons, we find that

- The CCSM3 thickness distribution differs qualitatively from the observationally derived thickness distribution produced by the offline sea ice model. The sea ice pattern generated by observationally derived forcings has the thickest ice along the coastline of northwestern Greenland and the Canadian Archipelago, with thickness decreasing outward across the basin in all directions (Fig. 4, left column). At both resolutions, the model produces an annual-mean pattern in which thickness is fairly uniform in a corridor stretching across the Arctic basin from the Canadian Archipelago to eastern Siberia, with a concentrated ice pile up near Wrangell Island on the Siberian side (Fig. 1).
- When forced with CCSM3 surface winds, the offline model produces annual-mean sea ice patterns with thicker ice on the Siberian side than on the Canadian

side, in opposition to the pattern produced by observed winds. Thus, surface wind biases alone would be sufficient to produce a reversal of the thickness gradient across the basin in CCSM3 even if the model were able to accurately simulate the observed surface temperature distribution (Fig. 4, middle and right columns).

- The reversal of the cross-polar thickness gradient produced in the offline model is consistent with surface wind differences between the NCEP-NCAR reanalysis and the CCSM3 simulations. CCSM3 surface winds are generally directed more toward Siberia and away from Canada than their reanalysis counterparts (Figs. 2 and 3).
- The ice pile up around Wrangell Island in CCSM3 is more pronounced at T42 resolution than at T85. However, the T85 winds produce thicker ice along the Siberian coast in the offline model. Thus, we cannot conclude that the reduction in Siberian sea ice thickness at higher resolution is due to the mechanical effect of resolution-dependent surface wind biases. Our results suggest that differences in thermodynamic forcing must also play a role.
- Ice builds up along the Canadian coastline in the T85 integration as in the observationally derived thickness pattern (Figs. 1 and 4), but no comparable Canadian maximum occurs at T42. The offline simulations show a similar Canadian thickness discrepancy in the sea ice response to surface winds from the T85 and T42 integrations. In the offline model the discrepancy can be related to the direction and strength of the spring and summer winds, which are more anticyclonic in the T42 integration, and more strongly offshore along the Canadian coastline. The largest improvement in the T85 Arctic surface winds is the disappearance of the spurious summertime polar anticyclone of the T42 integration. This improvement in summer surface winds apparently plays a role in establishing the T85 ice thickness maximum along the Canadian coastline.

The second part of our study attempts to relate the biases in CCSM3 Arctic surface winds to the model's simulation of the large-scale atmospheric circulation. We examine key circulation fields, which are closely related to the high-latitude Northern Hemisphere surface winds. Our examination of the structure and dynamics of the large-scale circulation reveals that

- With the exception of the summer season, Arctic SLP is too low in CCSM3 at both resolutions, and the low bias is more pronounced at the higher resolution. In particular, the Beaufort high is extremely weak in the fall, winter, and spring seasons (Fig. 6).

- The three-dimensional zonally asymmetric circulation associated with the DJF Beaufort high, as revealed by plots of stationary eddy geopotential height from the NCEP–NCAR reanalysis, has an equivalent barotropic structure, with slight upward amplification and only a small intensification near the surface. Above the surface the high is distinct from the Siberian high, and the center of the high is not associated with the coldest surface or lower-tropospheric temperatures (Fig. 7). In the CCSM3 integrations, the highest DJF SLP is found along the Arctic coast of eastern Siberia, with a cold-core baroclinic vertical structure associated with the coldest lower-tropospheric temperatures at that latitude. This cold-core baroclinic structure suggests that the high is an extension of the Siberian high rather than a distinct Beaufort high (Fig. 8).
- Summertime (JJA) Arctic SLP is too high in the T42 integration, which has a local SLP maximum near the pole in association with the anticyclonic summer surface wind bias. The erroneous polar high is virtually eliminated in the T85 integration, as can be seen in plots of zonally averaged SLP (Fig. 9).
- The observed Arctic summer circulation is characterized by a well-known North Polar low, accompanied by surface westerlies that, in the zonal mean, are comparable in strength to the midlatitude westerlies (Fig. 9). In the NCEP–NCAR reanalysis, the Arctic westerlies are maintained by an Arctic Ferrel cell (Fig. 10a), with northward eddy momentum fluxes in the upper troposphere (primarily by low-frequency eddies) and a thermally indirect mean meridional circulation with rising motion at the pole. A poleward lobe of the upper-tropospheric jet extends into the domain of the Arctic Ferrel cell.
- Despite the elimination of the T42 polar SLP maximum, the T85 integration does not produce a well-defined polar low. The summertime Arctic Ferrel cell and poleward lobe of the Northern Hemisphere jet also do not appear in the T85 integration, and the surface winds do not show the coherent polar cyclone found in the reanalysis.

Our goal in presenting these findings is to offer constructive criticism, and in pursuit of that goal we have omitted a detailed discussion of the many ways in which CCSM3 is an improvement over its predecessors. For example, the thickness distribution in Fig. 1 is clearly preferable to the one reported by Weatherly et al. (1998, their Fig. 7a) for the earlier CSM, regardless of any flaws found here.

Our results suggest two goals for future model development: improved simulation of the Beaufort high, and

improved simulation of the summertime North Polar low. Questions naturally arise as to whether these are in fact reasonable, attainable goals. In particular, can we be sure that a better simulation of the large-scale circulation will necessarily improve the thickness distribution? Should we expect a state-of-the-art GCM to produce a realistic circulation over a relatively small region like the Arctic? For that matter, how important is a realistic simulation of the thickness distribution?

Regarding the last question, it could be argued that the mean sea ice thickness is more important than its spatial distribution, since the mean thickness is more closely associated with the polar amplification of climate change (Holland and Bitz 2003). Nevertheless, a realistic thickness distribution could be quite important for the export of sea ice into the North Atlantic. Most of the export occurs in the transpolar drift stream (e.g., Serreze et al. 1989, their Fig. 1), which transports ice preferentially from the Siberian Arctic into the North Atlantic along the west coast of Greenland. Putting the ice in the right place could thus be important for correctly simulating the export, which regulates the salinity (and hence the stability) in regions of oceanic convection and helps determine the location of the North Atlantic sea ice edge (e.g., Bitz et al. 2005). Serreze et al. (1989) have also argued that ice production in the Canada basin, which occurs in autumn as a consequence of cyclonic summertime winds, could be important for brine production and surface heat flux in that region.

As for the ability of coupled models to simulate the regional circulation of the Arctic, most climate models can produce a Beaufort high. In fact, the consensus SLP pattern in the AMIP simulations of Bitz et al. (2002) had a Beaufort high that was somewhat too strong. The problem is the sensitivity of the sea ice thickness to errors in the location and strength of the high. The ice thickness bias found here is similar to the one found by Bitz et al. (2002), even though the Beaufort high in their study was too strong rather than too weak (in their case, poor placement of the high was responsible for the thickness error). Thus, a relatively high degree of accuracy in the simulation of the Beaufort high will be necessary to prevent errors in the thickness distribution.

The summer circulation also poses a challenge for climate models. Since Reed and Kunkel (1960), the prevailing view has been that the polar low is a graveyard of storms, in which low SLP is maintained by the incursion and stagnation of cyclones from the Arctic front. Here we show that the surface circulation around the low is maintained against surface friction by transient momentum flux, a result that also emphasizes the role of the transients. It is reasonable to assume that the

transients will be simulated more accurately at higher resolution, although it is not clear how much resolution is required. For example, Lynch et al.'s (2001) study of the Alaskan Arctic frontal zone found that the frequency of frontal systems depended on the representation of Alaskan topography, simulated at 30-km resolution in their model. But it should also be noted that at both resolutions considered here, CCSM3 transient momentum fluxes are substantially stronger than their reanalysis counterparts throughout the northern extratropics. We believe that this bias should be addressed in conjunction with any attempt to improve the simulation of the summertime Arctic circulation.

*Acknowledgments.* This research was supported by the Office of Science (BER), U.S. Department of Energy, Grant DE-FG02-03ER63604 to E. DeWeaver. Support for C. Bitz was provided by the National Science Foundation under Grant ATM0004261. Computational facilities have been provided by NCAR. NCAR is supported by the National Science Foundation. In addition, we thank Drs. Steve Vavrus and Dan Vimont for their encouragement and insights.

#### REFERENCES

- Bitz, C. M., M. M. Holland, A. J. Weaver, and M. Eby, 2001: Simulating the ice-thickness distribution in a coupled climate model. *J. Geophys. Res.*, **106**, 2441–2464.
- , J. C. Fyfe, and G. M. Flato, 2002: Sea ice response to wind forcing from AMIP models. *J. Climate*, **15**, 522–536.
- , M. M. Holland, E. C. Hunke, and R. E. Moritz, 2005: Maintenance of the sea-ice edge. *J. Climate*, **18**, 2903–2921.
- Bourke, R. H., and R. P. Garrett, 1987: Sea-ice thickness distribution in the Arctic Ocean. *Cold Reg. Sci. Technol.*, **13**, 259–280.
- Boville, B., 1991: Sensitivity of simulated climate to model resolution. *J. Climate*, **4**, 469–485.
- Briegleb, B., and D. H. Bromwich, 1998: Polar climate simulation of the NCAR CCM3. *J. Climate*, **11**, 1270–1286.
- Collins, W. D., and Coauthors, 2006a: The Community Climate System Model version 3 (CCSM3). *J. Climate*, **19**, 2122–2143.
- , and Coauthors, 2006b: The formulation and atmospheric simulation of the Community Atmosphere Model version 3 (CAM3). *J. Climate*, **19**, 2144–2161.
- Dickinson, R., K. W. Oleson, G. B. Bonan, F. Hoffman, P. Thornton, M. Vertenstein, and Z.-L. Yang, 2006: The Community Land Model and its climate statistics as a component of the Community Climate System Model. *J. Climate*, **19**, 2302–2324.
- ECMWF, 1997: ERA description. ECMWF Re-Analysis Project Report Series, Vol. 1, European Centre for Medium-Range Weather Forecasts, 72 pp.
- Gates, W. L., 1992: AMIP: The Atmospheric Model Intercomparison Project. *Bull. Amer. Meteor. Soc.*, **73**, 1962–1970.
- Hack, J. J., J. M. Caron, G. Danabasoglu, K. W. Olson, C. M. Bitz, and J. E. Truesdale, 2006a: CCSM–CAM3 climate simulation sensitivity to changes in horizontal resolution. *J. Climate*, **19**, 2267–2289.
- , —, S. G. Yeager, K. W. Oleson, M. M. Holland, J. E. Truesdale, and P. J. Rasch, 2006b: Simulation of the global hydrological cycle in the CCSM Community Atmosphere Model (CAM3): Mean features. *J. Climate*, **19**, 2199–2221.
- Held, I. M., M.-F. Ting, and H. Wang, 2002: Northern winter stationary waves: Theory and modeling. *J. Climate*, **15**, 2125–2144.
- Hibler, W. D., and G. M. Flato, 1992: Sea ice models. *Climate System Modeling*, K. Trenberth, Ed., Cambridge University Press, 788 pp.
- Holland, M., and C. M. Bitz, 2003: Polar amplification of climate change in the coupled models. *Climate Dyn.*, **21**, 221–232.
- , —, E. C. Hunke, W. H. Lipscomb, and J. L. Schramm, 2006: Influence of the sea ice thickness distribution on polar climate in CCSM3. *J. Climate*, **19**, 2398–2414.
- Houghton, J. T., Y. Ding, D. J. Griggs, M. Noguer, P. J. van der Linden, X. Dai, K. Maskell, and C. A. Johnson, 2001: *Climate Change 2001: The Scientific Basis*. Cambridge University Press, 881 pp.
- Hurrell, J. W., J. J. Hack, A. Phillips, J. Caron, and J. Yin, 2006: The dynamical simulation of the Community Atmosphere Model version 3 (CAM3). *J. Climate*, **19**, 2162–2183.
- Kalnay, E., and Coauthors, 1996: The NCEP–NCAR 40-Yr Reanalysis Project. *Bull. Amer. Meteor. Soc.*, **77**, 437–471.
- Large, W. G., and G. Danabasoglu, 2006: Attribution and impacts of upper-ocean biases in CCSM3. *J. Climate*, **19**, 2325–2346.
- Lynch, A. H., A. G. Slater, and M. Serreze, 2001: The Alaskan Arctic frontal zone: Forcing by orography, coastal contrast, and the boreal forest. *J. Climate*, **14**, 4351–4362.
- Nigam, S., and E. DeWeaver, 2003: Stationary waves (orographically and thermally forced). *Encyclopedia of Atmospheric Sciences*, J. Holton, J. Pyle, and J. Curry, Eds., Elsevier, 2780 pp.
- Palmén, E., and C. W. Newton, 1969: *Atmospheric Circulation Systems*. Academic Press, 603 pp.
- Ramage, C. S., 1971: *Monsoon Meteorology*. Academic Press, 296 pp.
- Randall, D., and Coauthors, 1998: Status of and outlook for large-scale modeling of atmosphere–ice–ocean interactions in the Arctic. *Bull. Amer. Meteor. Soc.*, **79**, 197–219.
- Randall, W. J., and I. M. Held, 1991: Phase speed spectra of transient eddy fluxes and critical layer absorption. *J. Atmos. Sci.*, **48**, 688–697.
- Reed, R. J., and B. A. Kunkel, 1960: The Arctic circulation in summer. *J. Meteor.*, **17**, 489–506.
- Rigor, I. G., J. M. Wallace, and R. L. Colony, 2002: Response of sea ice to the Arctic Oscillation. *J. Climate*, **15**, 2648–2663.
- Rind, D., R. Healy, C. Parkinson, and D. Martinson, 1995: The role of sea ice in  $2 \times \text{CO}_2$  climate model sensitivity. Part I: The total influence of sea ice thickness and extent. *J. Climate*, **8**, 449–463.
- Serreze, M. C., and R. G. Barry, 1988: Synoptic activity in the Arctic Basin, 1979–85. *J. Climate*, **1**, 1276–1295.
- , —, and A. S. McLaren, 1989: Seasonal variations in sea ice motion and effects on sea ice concentration in the Canada Basin. *J. Geophys. Res.*, **94**, 10 955–10 970.
- , A. H. Lynch, and M. P. Clark, 2001: The Arctic front as seen in the NCEP–NCAR reanalysis. *J. Climate*, **14**, 1550–1567.

- Thorndyke, A. S., and R. Colony, 1982: Sea ice motion in response to geostrophic winds. *J. Geophys. Res.*, **87**, 5845–5852.
- Vinje, T., 2001: Fram Strait ice fluxes and atmospheric circulation: 1950–2000. *J. Climate*, **14**, 3508–3517.
- von Storch, H., and F. W. Zwiers, 2001: *Statistical Analysis in Climate Research*. Cambridge University Press, 484 pp.
- Walsh, J., and C. Crane, 1992: A comparison of GCM simulations of Arctic climate. *Geophys. Res. Lett.*, **19**, 29–32.
- Weatherly, J., B. P. Briegleb, W. Large, and J. Maslanik, 1998: Sea ice and polar climate in the NCAR CSM. *J. Climate*, **11**, 1472–1486.
- Yeager, S. G., W. G. Large, J. J. Hack, and C. A. Shields, 2006: The low-resolution CCSM2. *J. Climate*, **19**, 2545–2566.
- Zhang, J., D. Rothrock, and M. Steele, 2000: Recent changes in Arctic sea ice: The interplay between ice dynamics and thermodynamics. *J. Climate*, **13**, 3099–3114.